Light Responsive Hydrogel Microcrawlers, Powered and Steered with Spatially Homogeneous Illumination

Jindrich Kropacek[1], Charlie Maslen[1], Paolo Gidoni[2,3], Petr Cigler[4], Frantisek Stepanek[1], Ivan Rehor[1,4]*

Affiliations

1. University of Chemistry and Technology Prague, Faculty of Chemical Engineering,Technicka 5, 166 28 Prague 6, Czech Republic.

2. University of Udine, Polytechnic Department of Engineering and Architecture, Via delle Scienze 206, 33100 Udine, Italy

3. Institute of Information Theory and Automation of the Czech Academy of Sciences, Pod vodárenskou věží 4, 182 08, Prague 8, Czech Republic

4. Institute of Organic Chemistry and Biochemistry of the Czech Academy of Sciences, Flemingovo nam. 2, 160 00, Prague, Czech Republic

*Correspondence to ivan.rehor@vscht.cz

Keywords: Hydrogel, microrobot, light-driven, collective, photothermal actuation

ABSTRACT

Sub-millimeter untethered locomoting robots hold promise to radically change multiple areas of human activity such as microfabrication/assembly or healthcare. To overcome the associated hurdles of such a degree of robot miniaturization, radically new approaches are being adopted, often relying on soft actuating polymeric materials. Here we present light-driven, crawling microrobots, that locomote by a single degree of freedom actuation of their light-responsive tail section. The direction of locomotion is dictated by the robot body design and independent of the spatial modulation of the light stimuli, allowing simultaneous multidirectional motion of multiple robots. Moreover, we present a method for steering such robots by reversibly deforming their front section, using UV light as a trigger. The deformation dictates the robot locomotion, performing right- or left-hand turning when the UV is turned on or off respectively. The robots' motion and navigation are not coupled to the position of the light sources, which enables simultaneous locomotion of multiple robots, steering of robots and brings about flexibility with the methods to deliver the light to the place of robot operation.

INTRODUCTION

Micrometer scale structures that can be moved and controlled by a user (microrobots) have been proposed for applications such as micromanipulation, non-invasive surgery, drug delivery, and lab-on-

chip technologies[1–6]. In many of these applications, simultaneous operation of multiple robots is required. An ultimate goal is a group of active robots operating parallelly but independently so that they can efficiently complete the desired task in an analogy of a macroscopic robotic assembly line, or such robots could combine their forces to manipulate objects significantly bigger than themselves[7,8]. Hence, methods of microrobot control that enable their parallel independent operation is getting to the center of research interest.

Microrobotic systems can be divided into two categories by how the forces that drive their motion are applied. Forces can either be applied externally by means of magnetic[9,10], or acoustic fields[11]. Alternatively, they can arise locally from interactions between the microrobots body and their environment, as in the case of shape-changing (actuating) microrobots (crawling[12–17], swimming[18–22], jumping[23]), or propulsion-based microrobots[24,25].

Locomotion by external fields allows for control of large samples of microrobotic swarms, however, each microrobot within the swarm experiences the same forces and so generally moves in the same direction or with the same behavior. Advancements in magnetic field-driven microrobotics have demonstrated their ability to exhibit independent behaviors, but require the use of heterogeneous swarms or complex external hardware[26–30]**.** For locomotion by actuation or propulsion, the behavior of the microrobot is governed by its current state and the state of its local environment, hence, it offers potential for each microrobot to act independently within a group. In many cases of propulsion-driven microrobots the source of energy is typically dispersed within the environment as chemical fuel and individual microrobots move independently within a large group (neglecting fluidic interactions between microrobots). Similarly, dispersion of nutrients (chemical fuel) enables independent locomotion within a group of biohybrid microrobots relying on actuating cells as a source of motion[20,22,31,32]. However, in these cases the microrobots behavior is driven by a supply of energy that cannot easily be switched on and off, making such mechanisms for robot control limited to predefined arrangements of fuel gradients and, thus, cumbersome. An energy source that can be easily controlled both spatially and temporally is light. Used in conjunction with photo-responsive materials, light has been used to induce the locomotion of microrobots that respond to the absorption of light energy by shape changes[13,15,16,19,33–35]. These shape changes result in net forces being applied locally to the surroundings by the microrobot, and, hence, if the process can be induced simultaneously in large groups of microrobots, the microrobots will act independently within the group[3].

Achieving locomotion by shape changes in the micro-regime is not straightforward. The sub-millimeter robotic systems are mostly operated in fluidic environments to suppress the dominance of

adhesive forces, which hinder any motion over the substrate. Such robots, with dimensions < ~1 mm, typically move in liquids in the low Reynolds number regime. Here, viscous forces dominate over inertial forces and, thus, directional motion is provided only by non-reciprocal, cyclic shape changes[36]. Alternatively, other phenomena can be exploited to break symmetry within a single degree of freedom (DOF) actuation cycle to provide directional motion, such as asymmetric friction[13,15,17,33]. Multiple microrobot designs have been reported that mimic non-reciprocal gaits utilized by various organisms, where light was used to control the actuation, being localized to induce shape changes at specific regions of the microrobot[14,19,35]. In these cases, the resulting locomotion direction is dictated by the spatial/spatiotemporal light distribution, such as focused beam localization or light pattern travelling direction. Multiplying such illuminating schemes to simultaneously drive multiple robots in arbitrary directions would require accordingly complex illumination setups, with the level of complexity increasing with every robot added to the system. Hence, it would be preferred to have microrobots that, when illuminated with light of spatially uniform intensity, undergo shape transformations that result in net displacements. This is not an easy approach, as is witnessed by sparse evidence of its experimental microrobotic realizations. It has been demonstrated in swimming hydrogels that undergo non-reciprocal shape changes owing to out-of-equilibrium actuation of their helical bodies[18] and crawling liquid crystal elastomers with asymmetrical frictional properties[33]. Moreover, for successful application of such microrobots, these must not only provide continuous net displacement but also their direction of motion must be controllable.

In this research, we present hydrogel microrobots that display directional motion in response to a homogeneous illumination source. The hydrogels undergo reciprocal actuation, which is coupled to a friction hysteresis between shrinking and expanding phases. The head-tail asymmetry, required for the net displacement of the microrobots, is provided by material heterogeneity of the microrobot's body, with only the tail section of the body being responsive to light. Introducing this asymmetry removes the need for spatial localization of light and allows multiple microrobots to locomote by a global light source. Furthermore, we demonstrate the ability to steer the microrobots by appending a simple pH-responsive hydrogel block to the microrobot body. This block collapses and re-swells, asymmetrically, upon a photoinduced pH change. The change in the robot's left-right symmetry induced by this volumetric response controls its trajectory.

MATERIALS AND METHODS

N-isopropyl acrylamide (NIPAM), poly(ethylene glycol) diacrylate (average M_n = 700 Da) (PEGDA), *N,N'*-methylenebisacrylamide (MBAAm), poly(ethylene glycol) (average M_n = 200 Da) (PEG 200),

acrylic acid (AA), lithium phenyl-2,4,6-methyl benzoyl phosphinate (LAP), Darocur 1173, trisodium citrate, poly(ethylene glycol) methyl ether thiol (average M_n = 6000 Da) (PEG-thiol), Tween 20, Pluronic F-127 and pyranine were purchased from Sigma Aldrich. Tetrachloroaurate trihydrate was purchased from Alfa Aesar. Sylgard® 184 elastomer kit (PDMS base and curing agent) was purchased from Dow Corning. All chemicals were purchased in standard purities as provided and used as received. Reverse osmosis water (MilliQ) was used for all experiments (18.2 MΩ at 25 °C). 1% w/w gold nanosphere (diameter 15 nm) colloidal solution was prepared using the citrate method reported in[40] and subsequently incubated with 0.01% w/w PEG-thiol (ref.[37]). Gold nanorods with longitudinal plasmon resonance around 800 nm were prepared using seed-mediated method[41].

Precursor solutions

Standard photoresponsive NIPAM hydrogel precursor was prepared as described previously (ref.[13,37]) by dissolving 37 mg NIPAM, 2.5 mg LAP, and 20 µL PEGDA in 100 µL of gold nanosphere solution. The more light-sensitive NIPAM hydrogel was prepared by dissolving 48 mg NIPAM, 8 mg MBAAm, and 1.5 mg of LAP in 100 µL PEG 200 and 30 µL of gold nanorods solution. Non-responsive PEGDA hydrogel precursor was prepared by dissolving 2.5 mg LAP in a mixture of 60 mg PEGDA and 140 µL water. pH-responsive AA hydrogel precursor was prepared by dissolving 55 mg NIPAM, 25 mg MBAAm, and 1 mg LAP in a mixture of 182 µL of 25 % w/w Sodium Acrylate solution in water (pH adjusted to 7 with sodium hydroxide) and 138 mg PEG 200. All components of a particular precursor solution were mixed together, sonicated for 5 mins in a bath and subsequently centrifuged at 1000 rcf for 1 min to remove dust contamination.

Microrobot Synthesis

Microrobots were produced using the multi-stream stop-flow lithography technique described in[42]. Briefly: precursor solutions were introduced in 2 or 3 separate inlets and pumped into a microfluidic channel (400 µm wide, 30 µm deep). With the pressure removed, and flow stopped, UV light was focused through a photomask inducing polymerization of the precursor in a region defined by the photomask. The position and orientation of the photomask with respect to the laminar flows of the precursors was set to achieve the desired microrobot constitutions. After production, the channel was purged with 0.5% w/w Tween 20 solution and the microrobots were collected in PCR tubes. The sample was washed 4 times with fresh Tween 20 solution by sedimentation of the microrobots, removal of the supernatant, and replacement with fresh Tween 20 solution. 'T'-shaped microrobots were subsequently transferred into mercaptoethanol (10 % v/v), Darocur 1173 (1 % v/v), and ethanol (89 % v/v) solution, kept under UV lamp for 2 hours to remove remaining acrylates (reason of which is discussed in Supplementary text S3) and were subsequently washed.

Microrobot Actuation

Polystyrene lids of 96-well plates (purchased from Thermo Fisher Scientific) were used as wells for crawling experiments. Produced microrobots were sedimented in these circular, 0.3 mm high wells having 4 mm in diameter. Wells were then filled with aqueous surfactant solutions and covered with glass slide. The surfactant solution for bimaterial crawlers was Tween 20 (0.5 % w/w), as in ref.[13]. For the pH-responsive steering, Pluronic (5 % w/w) was used. All experiments were performed with a Nikon Ti-U inverted microscope. For photo-induced pH change, 1 % w/w of pyranine in 5% Pluronic solution was used. For the high area global illumination experiments, a 3W NIR 808 nm laser diode was aimed directly at the sample with microrobots under the inline 45°, to avoid the transmitted light entering the objective. In the pH-steering experiments, a 1W green 532 nm laser diode was aimed to the sample using a custom-made setup comprising a 420 nm shortpass dichroic mirror and a shutter (Figure S5). When the shutter was opened, the laser beam was reflected by the dichroic mirror to the condenser lens (Figure S5). By changing the height of the condenser lens, the laser beam focus was adjusted to provide sufficient intensity for full contraction of crawlers, and with the spot size exceeding the dimensions of the crawler. Color filter was placed directly at the top of the objective to absorb the laser beam and prevent it from entering the objective. With 'T'-shaped microrobots, the setup described above was used for their actuation while episcopic UV illumination was used for pyranine excitation and the associated pH decrease and microrobot shape change.

RESULTS

Head-tail symmetry breaking

In our previous research, we induced directional motion with prismatic[13] or disk-shaped[37] microgels by light-induced 1 DOF actuation comprising isotropic shrinkage and expansion of a section of their body. The microrobots are composed of thermo-responsive poly-*N*-isopropyl acrylamide (PNIPAM), made photo-responsive by the incorporation of gold nanoparticles. When a section of the robot body is illuminated by focused laser light, this section heats up, resulting in local shrinkage of the illuminated gel area. Upon cyclic pulse illumination, the rapid, out-of-equilibrium, shrinking and expansion processes yield a hysteresis in the properties of the surface of the gel which is exhibited as non-reciprocally varying friction coefficients between the gel and the surface. The result is a net displacement of the microrobot after each shrinking-expanding cycle, along the symmetry axis of the deformed body in the direction from the center of irradiation to the geometrical center of the shape.

Since illumination localization is responsible for the crawling direction, the use of unfocused light would result in isotropic actuation of an entire crawler and, hence, no net displacement over one actuation cycle. To remove the need for spatial localization of the beam spot, we broke the head-tail symmetry of the crawler's response to the light stimulus. To do that, we fabricated microgels (150 µm x 50 µm), composed of two segments – 'tail' (photo-responsive PNIPAM), and 'head' (non-responsive poly(ethylene glycol) diacrylate = PEGDA) **(Figure 1).** When these crawlers are subjected to pulse illumination with a laser of a spot size exceeding the crawler size, their responsive segment exhibits actuation while the non-responsive segment volume remains unaffected by the illumination. This arrangement results in crawler motion. The friction coefficient between the PEGDA segment and the surface remains constant over the course of the actuation cycle, while that of the PNIPAM segment changes non-reciprocally, which results in the net displacement of the crawler. During collapse, the friction coefficient of the PNIPAM significantly decreases, below the value of PEGDA **(Figure S1),** and hence, the collapsing PNIPAM segment retracts towards the microrobot center (analogously to our previously described solely PNIPAM crawler). During subsequent expansion, the PNIPAM friction coefficient steeply rises above the value of PEGDA and, hence, the PNIPAM segment acts as an anchoring point, pushing the PEGDA section forward. The result is a net displacement of ~9 µm during one cycle **(Figure 2A).**

To increase the illuminated area in which actuation (and concomitantly crawling) can be achieved, we optimized the previously used composition of the responsive section of the microgels to achieve a sharp volumetric transition at the lower critical solubility temperature (LCST). Furthermore, we increased the laser power from 200 mW to 3 W. With these changes we achieved a 25-fold increase of the active area (from ~0.03 to ~0.8 mm^2 (Details in supplementary text S1)). All microrobots within the illuminated area display the same behavior, simultaneously crawling in the direction given by the orientation of their active and passive sections (Figure 1B). The crawling direction of the individual crawlers is independent of their position and orientation with respect to the center of illumination, they crawl along straight trajectories and when two crawlers hit each other, they can push each other.

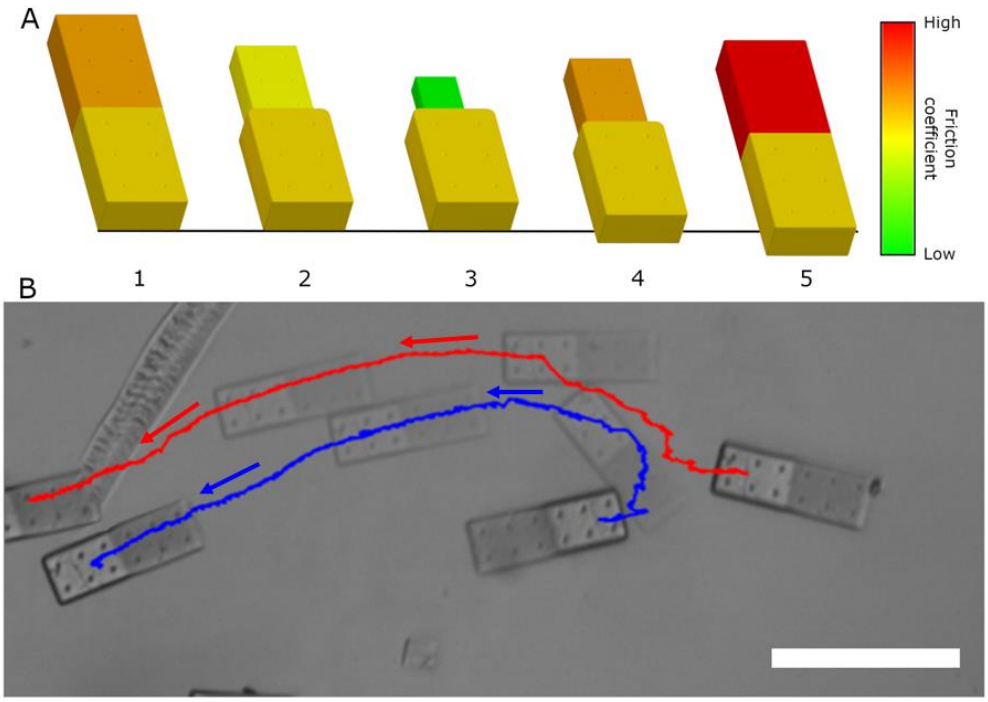

Figure 1. A – Schematic representation of friction hysteresis-based locomotion. The friction coefficient of the actuating segment changes non-reciprocally along the actuation cycle, dropping steeply during the collapse phase, and rising steeply during the expansion phase, which results in a net displacement over the course of a cycle. The scheme displays a first cycle of a sequence, where the PNIPAM gel starts contracting from the equilibrium state. For consecutive cycles, the picture 1 is to be replaced by the picture 5 (more details in ref.[13]) B – Two crawlers actuated simultaneously and crawled from their original position in the direction of their PEGDA segment (bright) i.e. towards each other. Consequently, they meet each other and as a result of their physical interaction, they align their orientations and continue in the same direction. Note – the laser position has not been changed throughout the entire course of the experiment. The scale bar corresponds to 200 µm.

Locomotion of bimaterial crawlers

The embedding of the head-tail asymmetry in the geometry of the hydrogel crawler, instead of relying on spatial localization of the irradiation, allows a more proper analysis of the effectiveness of different designs of crawler.

Our investigation focused on the effects of the ratio *R/L* between the length of the passive, PEGDA segment, *R*, and the length of the active, PNIPAM one, *L*. We developed a theoretical model of the crawler, discussed in detail in Supplementary Text S2, and fabricated a series of crawlers with different active-passive ratios.

The results are summarized in Figure 2, where we represent the displacement per irradiation cycle as a fraction of the length of the active segment. The displacement is clearly null for *R/L*=0 (only PNIPAM), but then increases steeply, reaching a plateau for ratios greater than *R/L*=2/3, corresponding to a displacement per actuation cycle of the order of 0.15 times the length L of the active segment. A comparable performance is then sustained for increasingly larger values of the ratio *R/L*, up to *R/L*=5 and, theoretically, above. We investigated this experimentally only up to *R/L*=5 because we could produce maximally 300 μm long robots, being limited by the maximum achievable width of a microfluidic channel during the synthesis.

The ability to push large passive front segments *via* relatively small active segment is particularly relevant, since the passive section of a robot does not need to serve just as an 'anchor' to simply break the head-tail symmetry of the crawler, but it can accommodate further robot functions. Indeed, our design is suitable for integration with additional, bulky functional regions that can be appended to the front without losing, nor significantly penalizing, the robot crawling ability.

We observed inconsistencies in the displacement per irradiation cycle for every crawler, reflected by the large standard deviation error bars. We attribute this to microscopic defects on the polystyrene surface, as well as subtle inhomogeneities in the illumination conditions (point-spread function of the beam, flickering of the laser). Despite such variability and the complexity of the phenomenon, we are able, with a basic model, to capture the main effect inducing the locomotion of the microrobot and to qualitatively predict the trend for increasing ratios *R/L*. As we discuss partially in Figure 2 and further in Supplementary text S2, the observed variability in deformation and friction, although affecting quantitatively our prediction, maintains nonetheless a similar overall predicted behavior compatible with experimental data.

The most interesting variation occurs in the value of the ratio *R/L* maximizing the rescaled displacement per cycle: the optimum is quite sensitive to the maximum friction coefficient μ_{max} obtained by PNIPAM in the cooling phase, whose value could be only partially estimated by sliding data since it corresponds to excessively slow speeds. Although the performance plateau is present for all admissible values of μ_{max}, the performance peak observed around *R/L*=2 is compatible only with a smaller range, thus improving our previous estimate on the coefficient (see Supplementary text S2 and Figure S2).

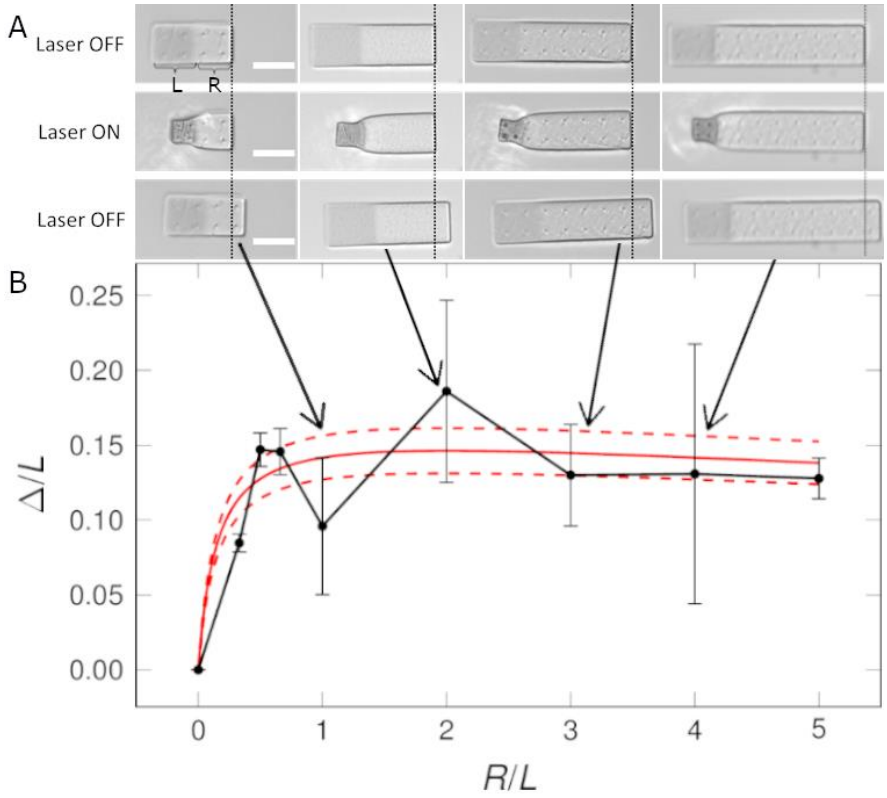

Figure 2. A – Displacements of rectangular microrobots of varying aspect ratios during one shrinking-expanding cycle. The active, gold–loaded PNIPAM segment dimensions are always 50 × 50 µm, while the passive PEGDA region length varies from 50 to 200 µm. All the crawlers provide directional motion upon cyclic illumination. Scale bar = 50 µm. B – Displacement Δ produced in one cycle rescaled with respect to the length of the active segment L, plotted in terms of the ratio *R/L* between the lengths *R* of the PEGDA segment and L of the PNIPAM segment (at room temperature). The black graph shows the experimental data, the red solid line our model prediction and the two red dashed lines the changes in our prediction for one standard variation in the maximum contraction of the PNIPAM segment.

Robot Steering

To enable steering of the microrobots without the need for localization of the stimulus, we appended a pH-responsive polyacrylic acid (PAA) segment to the robot head through simple modification of the stop-flow lithography fabrication procedure. Thus, steerable microrobots are composed of three gel segments – PNIPAM, PEGDA, and PAA – distributed as parallel stripes within the robot 'T'-shape **(Figure 3).** The stripe orientation is slightly tilted with respect to the front edge of the 'T'-shape. Therefore, one arm of the 'T'-shape consists predominantly of the PEGDA gel, while the other consists of the PAA gel. When swollen, the PAA gel exhibits greater friction than the PEGDA,

when sheared along the substrate (Figure S1). Thus, the center of friction (see Supplementary text S2 and ref.[38] for detailed definition) of this front side is offset from the main left-right axis of the crawler towards the PAA arm. The forward force (F_{CR} in Figure 3) – realized by the expanding PNIPAM segment – acts along the main left-right axis of the crawler, while the counteracting friction force (F_{FR} in Figure 3) is localized at the offset center of friction. As a result, a torque emerges between these two forces, and this torque is responsible for the forward motion of the crawler along a circular path in the direction of the PAA arm.

The PAA shows pH-dependent volumetric change, collapsing to approximately 40 % of its original linear dimensions at a pH of 3.2 (Figure S3). In the collapsed state, only the PAA segment of the crawler is shrunk. Since its collapse is isotropic in *x*, *y* and, crucially, *z* direction, the PAA segment retracts from the surface and only the PEGDA segment remains in contact (Figure S4). Hence, the center of friction gets shifted to the PEGDA arm side and causes the robot to follow a curved path in the opposite direction i.e. towards the PEGDA arm side (Figure 3). The inverse volumetric change can be achieved by incorporating a basic monomer into the gel structure (e.g. 2-dimethylaminoethyl acrylate) instead of acrylic acid. Similarly, the pH range in which the volumetric change occurs does not need to be the same as we mentioned above, but it can be shifted by compositional changes of gel´s precursor solution.

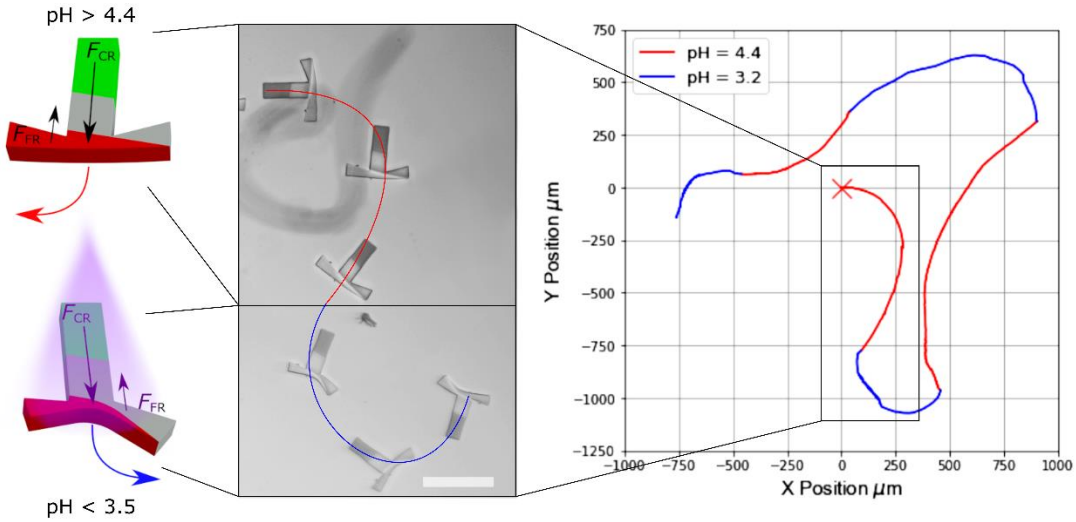

Figure 3. Crawler trajectory can be controlled by UV illumination of the experimental area. The rear end of the robot (green) is composed of gold-loaded PNIPAM and is responsible for its locomotion. The front side of the robot contains a segment of a pH-responsive gel (red), positioned slightly asymmetrically with respect to the robot's left-right symmetry. The greater friction of the pH-responsive section means the robot's center of friction is shifted to the right-hand side from the central left-right axis and the robot crawls along a curved trajectory (red lines). UV illumination of the

solution around the robot causes a drop in the solution pH, which results in the deformation of the pH-responsive segment away from the surface. The deformation moves the center of friction to the left-hand side from the robot's left-right symmetry axis, reversing the direction of the robots curved path (blue lines). The turning direction can be switched repeatedly by changing pH of surrounding solution (blue/red lines in the plot). The microscopy image is a montage of several images, displaying the robot's consecutive positions in time. The scale bar corresponds to 200 μm.

To change the pH remotely, without disturbing the environment, a photoacid pyranine was dissolved in the solution. Under illumination with UV light, pyranine is excited, which decreases its pK_a, causing a decrease in pH[39] (Supplementary text S3). In this experiment, the robot was steered and powered by two global illumination sources – the defocused, 532 nm laser served as a power source for its actuation while 400 nm UV light was used to excite the pyranine, collapse the PAA segment and change the direction of robot's locomotion. When left in the dark, the pyranine gradually relaxes back to its ground state, which is reflected in the pH increase. To deal with slow kinetics of this relaxation as well as partial photodegradation of pyranine (Supplementary text S3), we replaced part of the solution during this step with a fresh one. This returned the robot to its original shape and its original trajectory (in the direction of the PAA arm) was re-established. Alternating the respective low and high pH periods allowed us to navigate the robot over the substrate (Figure 3). We consider the presented single DOF steering system, with alternating left/right turning, a promising steering strategy, since accumulation of more DOFs in soft microrobots is inherently complicated. Similar 1 DOF strategy, relying on alternating left-right turning to achieve the desired direction, has been used to steer early remote controlled solid wing flying models, due to the cost of radio-controlled servo motors.

CONCLUSION

We present a soft light-powered and steered microrobot, that does not require spatial modulation of light for operation. The direction of robot motion is not coupled to the illumination position and proceeds along a straight line following the vector active segment – passive segment. This enables omnidirectional parallel motion of multiple robots found in the illuminated area. The experiments as well as theoretical analysis showed that even a small active segment is sufficient for moving a large front passive segment ($R/L = 5$). This enables the incorporation of further functionalities into the robot. We demonstrate a steering functionality, where a microrobot turning direction can be switched between left- and right-handed just by on/off UV illumination. As in the case of the actuation light source, the UV light does not need to be focused. This together provides a system, with no

constraints on the spatial distribution of the light sources, which firstly enables simultaneous operation of multiple robots and, secondly, may provide flexibility to the way light is brought to the robot. We believe that our approach may allow the operation of light-controlled robots outside strictly defined microscopic setups, where the light will be delivered to the robot by, for example, optical fibers.

Acknowledgement

P.G. acknowledges the GAČR Junior Star Grant 21-09732M, I.R. acknowledges the UCT Dagmar Prochazkova starting grant.

References

1. Sitti M, Ceylan H, Hu W, et al. Biomedical Applications of Untethered Mobile Milli/Microrobots. Proceedings of the IEEE 2015;103(2):205–224; doi: 10.1109/JPROC.2014.2385105.

2. Ceylan H, Giltinan J, Kozielski K, et al. Mobile microrobots for bioengineering applications. Lab on a Chip 2017;17(10):1705–1724; doi: 10.1039/C7LC00064B.

3. Palagi S, Singh DP, Fischer P. Light-Controlled Micromotors and Soft Microrobots. Advanced Optical Materials 2019;1900370; doi: 10.1002/adom.201900370.

4. Zhang H, Hutmacher DW, Chollet F, et al. Microrobotics and MEMS-Based Fabrication Techniques for Scaffold-Based Tissue Engineering. Macromol Biosci 2005;5(6):477–489; doi: 10.1002/mabi.200400202.

5. Jang D, Jeong J, Song H, et al. Targeted drug delivery technology using untethered microrobots: a review. J Micromech Microeng 2019;29(5):053002; doi: 10.1088/1361-6439/ab087d.

6. Nauber R, Goudu SR, Goeckenjan M, et al. Medical microrobots in reproductive medicine from the bench to the clinic. Nat Commun 2023;14(1):728; doi: 10.1038/s41467-023-36215-7.

7. Wang Q, Zhang L. External Power-Driven Microrobotic Swarm: From Fundamental Understanding to Imaging-Guided Delivery. ACS Nano 2021;15(1):149–174; doi: 10.1021/acsnano.0c07753.

8. Wu R, Zhu Y, Cai X, et al. Recent Process in Microrobots: From Propulsion to Swarming for Biomedical Applications. Micromachines 2022;13(9):1473; doi: 10.3390/mi13091473.

9. Floyd S, Diller E, Pawashe C, et al. Control methodologies for a heterogeneous group of untethered magnetic micro-robots. The International Journal of Robotics Research 2011;30(13):1553–1565; doi: 10.1177/0278364911399525.

10. Tung HW, Maffioli M, Frutiger DR, et al. Polymer-Based Wireless Resonant Magnetic Microrobots. IEEE Transactions on Robotics 2014;30(1):26–32; doi: 10.1109/TRO.2013.2288514.

11. Aghakhani A, Yasa O, Wrede P, et al. Acoustically powered surface-slipping mobile microrobots. Proceedings of the National Academy of Sciences 2020;117(7):3469–3477; doi: 10.1073/pnas.1920099117.

12. Maeda S, Hara Y, Sakai T, et al. Self-Walking Gel. Advanced Materials 2007;19(21):3480–3484; doi: 10.1002/adma.200700625.

13. Rehor I, Maslen C, Moerman PG, et al. Photoresponsive Hydrogel Microcrawlers Exploit Friction Hysteresis to Crawl by Reciprocal Actuation. Soft Robotics 2020; doi: 10.1089/soro.2019.0169.

14. Miskin MZ, Cortese AJ, Dorsey K, et al. Electronically integrated, mass-manufactured, microscopic robots. Nature 2020;584(7822):557–561; doi: 10.1038/s41586-020-2626-9.

15. Zhu QL, Du C, Dai Y, et al. Light-steered locomotion of muscle-like hydrogel by self-coordinated shape change and friction modulation. Nat Commun 2020;11(1):5166; doi: 10.1038/s41467-020-18801-1.

16. Reynolds MF, Cortese AJ, Liu Q, et al. Microscopic robots with onboard digital control. Science Robotics 2022;7(70):eabq2296; doi: 10.1126/scirobotics.abq2296.

17. Sun X-C, Xia H, Xu X-L, et al. Ingenious humidity-powered micro-worm with asymmetric biped from single hydrogel. Sensors and Actuators B: Chemical 2020;322:128620; doi: 10.1016/j.snb.2020.128620.

18. Mourran A, Zhang H, Vinokur R, et al. Soft Microrobots Employing Nonequilibrium Actuation via Plasmonic Heating. Adv Mater 2017;29(2):n/a-n/a; doi: 10.1002/adma.201604825.

19. Palagi S, Mark AG, Reigh SY, et al. Structured light enables biomimetic swimming and versatile locomotion of photoresponsive soft microrobots. Nat Mater 2016;15(6):647–653; doi: 10.1038/nmat4569.

20. Aydin O, Zhang X, Nuethong S, et al. Neuromuscular actuation of biohybrid motile bots. PNAS 2019;116(40):19841–19847; doi: 10.1073/pnas.1907051116.

21. Khalil ISM, Tabak AF, Seif MA, et al. Controllable switching between planar and helical flagellar swimming of a soft robotic sperm. PLOS ONE 2018;13(11):e0206456; doi: 10.1371/journal.pone.0206456.

22. Magdanz V, Sanchez S, Schmidt OG. Development of a Sperm-Flagella Driven Micro-Bio-Robot. Advanced Materials 2013;25(45):6581–6588; doi: 10.1002/adma.201302544.

23. Li M, Wang X, Dong B, et al. In-air fast response and high speed jumping and rolling of a light-driven hydrogel actuator. Nature Communications 2020;11(1):3988; doi: 10.1038/s41467-020-17775-4.

24. Hu W, Ishii KS, Fan Q, et al. Hydrogel microrobots actuated by optically generated vapour bubbles. Lab Chip 2012;12(19):3821–3826; doi: 10.1039/c2lc40483d.

25. Sharan P, Maslen C, Altunkeyik B, et al. Fundamental Modes of Swimming Correspond to Fundamental Modes of Shape: Engineering I-, U-, and S-Shaped Swimmers. Advanced Intelligent Systems 2021;3(11):2100068; doi: 10.1002/aisy.202100068.

26. Zhu S, Zheng W, Wang J, et al. Interactive and synergistic behaviours of multiple heterogeneous microrobots. Lab on a Chip 2022; doi: 10.1039/D2LC00265E.

27. Diller E, Miyashita S, Sitti M. Remotely addressable magnetic composite micropumps. RSC Adv 2012;2(9):3850–3856; doi: 10.1039/C2RA01318E.

28. Floyd S, Diller E, Pawashe C, et al. Control methodologies for a heterogeneous group of untethered magnetic micro-robots. The International Journal of Robotics Research 2011;30(13):1553–1565; doi: 10.1177/0278364911399525.

29. Pawashe C, Floyd S, Sitti M. Multiple magnetic microrobot control using electrostatic anchoring. Appl Phys Lett 2009;94(16):164108; doi: 10.1063/1.3123231.

30. Sitti M, Wiersma DS. Pros and Cons: Magnetic versus Optical Microrobots. Advanced Materials 2020;32(20):1906766; doi: 10.1002/adma.201906766.

31. Alapan Y, Yasa O, Yigit B, et al. Microrobotics and Microorganisms: Biohybrid Autonomous Cellular Robots. Annual Review of Control, Robotics, and Autonomous Systems 2019;2(1):205–230; doi: 10.1146/annurev-control-053018-023803.

32. Bastos-Arrieta J, Revilla-Guarinos A, Uspal WE, et al. Bacterial Biohybrid Microswimmers. Front Robot AI 2018;5; doi: 10.3389/frobt.2018.00097.

33. Zeng H, Wasylczyk P, Parmeggiani C, et al. Light-Fueled Microscopic Walkers. Advanced Materials 2015;27(26):3883–3887; doi: 10.1002/adma.201501446.

34. Francis W, Dunne A, Delaney C, et al. Spiropyran based hydrogels actuators—Walking in the light. Sensors and Actuators B: Chemical 2017;250:608–616; doi: 10.1016/j.snb.2017.05.005.

35. Rogóż M, Zeng H, Xuan C, et al. Light-Driven Soft Robot Mimics Caterpillar Locomotion in Natural Scale. Advanced Optical Materials 2016;4(11):1689–1694; doi: 10.1002/adom.201600503.

36. Purcell EM. Life at low Reynolds number. American Journal of Physics 1977;45(1):3–11; doi: 10.1119/1.10903.

37. Vrba J, Maslen C, Maxova J, et al. An automated platform for assembling light-powered hydrogel microrobots and their subsequent chemical binding. Journal of Computational Science 2021;55:101446; doi: 10.1016/j.jocs.2021.101446.

38. Vakkipurath Kodakkadan YN, Maslen C, Cigler P, et al. Friction-directed self-assembly of Janus lithographic microgels into anisotropic 2D structures. Journal of Materials Chemistry B 2021;9(23):4718–4725; doi: 10.1039/D1TB00572C.

39. Sandoval C, Ortega A, Sanchez S, et al. Structuration in the Interface of Direct and Reversed Micelles of Sucrose Esters, Studied by Fluorescent Techniques. PloS one 2015;10:e0123669; doi: 10.1371/journal.pone.0123669.

40. FRENS G. Controlled Nucleation for the Regulation of the Particle Size in Monodisperse Gold Suspensions. Nature Physical Science 1973;241(105):20–22; doi: 10.1038/physci241020a0.

41. Nikoobakht B, El-Sayed MA. Preparation and Growth Mechanism of Gold Nanorods (NRs) Using Seed-Mediated Growth Method. Chem Mater 2003;15(10):1957–1962; doi: 10.1021/cm020732l.

42. Appleyard DC, Chapin SC, Srinivas RL, et al. Bar-coded hydrogel microparticles for protein detection: synthesis, assay and scanning. Nat Protoc 2011;6(11):1761–1774; doi: 10.1038/nprot.2011.400.

Supplementary information

Light Responsive Hydrogel Microcrawlers, Powered and Steered with Spatially Homogeneous Illumination

*Jindrich Kropacek[1], Charlie Maslen[1], Paolo Gidoni[2], Petr Cigler[3], Frantisek Stepanek[1], Ivan Rehor[1,3]**

Content:

Supplementary text S1: Increasing area of actuation

The light intensity drops linearly with the illuminated area (i.e. with a square of the area diameter) and, thus represents the bottleneck for collective light-powered robot actuation. In the following section, we describe the optimization of the microrobot sensitivity toward light illumination, which allowed their collective actuation in the area of ~0.8 mm^2. Stretching the area by a mere increase of the laser power would be unsafe and impractical, thus we coupled it to the change of the absorbing species and optimization of the temperature-induced collapse properties of the gel. Gold nanorods, used instead of currently used gold nanospheres, have longitudinal plasmonic band shifted to wavelength around 800 nm (ref.[1]), which is advantageous since affordable powerful NIR laser diodes can be easily purchased, which keeps our microscopic setup affordable and easy to install in any lab. The nanorods were synthesized according to standard procedure (ref.[1]), the 20.5 mL of the resulting nanorod colloid was washed twice with water (to 1 % of original concentration of CTAB), and incubated with 3 mg of PEG-thiol (ref.[2]) and subsequently concentrated to 30 µL, to be used in the pre-gel identically as gold nanospheres.

Next, we steepened the robot's volumetric response to the temperature changes, by replacing the hydrophilic PEGDA crosslinker with *N,N'*-methylenebisacrylamide (MBAAm). Since the PEGDA remained hydrophilic even at elevated temperatures, it was hindering the gel collapse. PEGDA-crosslinked PNIPAM gels thus exhibited a gradual collapse occurring between 30 and 80 °C. By replacing the PEGDA crosslinker with MBAAm, the hydrogel reaches an almost completely collapsed state at 40 °C **(Figure S6).** However, this comes at a cost of increasing the time of re-swelling, it takes ~5 s to re-swell compared to ~1.2 s (for 100 µm squares), which results in somewhat slower microrobots locomotion. The above-described changes in the robot composition and illumination resulted in a 25-fold increase of the active area to ~0.8 mm^2, compared to the previously published design (ref.[2]). Notably, these composition changes go along with the design, previously described by others (ref.[3]).

Supplementary text S2: Microgel-substrate friction and locomotion model for multi-material crawlers

Microgel-substrate friction

The friction force acts at every point of the sheared surface and depends on the local friction coefficient. A mean location of the distribution of friction over the sheared plane provides a point, we call 'center of friction (C_{Fr})' in an analogy to the center of mass (C_M). The resulting friction force exerted on the gel is allocated to this point. For uniform composition surfaces, the C_{Fr} is identical to C_M. However, for surfaces, composed of more materials these two do not match (ref.[4]). In the case of the asymmetric 'T'- shaped crawler, at high pH (pH = 4.4), i.e., in the swollen state, the PAA exhibits greater friction than the PEGDA and thus the center of friction is offset from the main left-right axis in the direction towards the PAA arm. Hence a torque emerges between the forward force of the expanding crawler 'tail' and the opposing friction force. As a result, the crawler follows a curved path in the direction of the PAA arm.

We previously developed a method, to indirectly measure the frictional properties of the various compositions (PAA, PEGDA, PNIPAM) (ref.[2]). Briefly, disk-shaped microgels (100 µm diameter) of homogenous compositions were allowed to slide down an inclined (10°) surface. The velocity of the sliding disks is inversely proportional to the frictional forces between the gel and the surface (ref.[2]). The frictional properties of PNIPAM have already been studied in (ref.[2]): the sliding velocity *u(t)* of a PNIPAM disk subjected to a heating-cooling cycle shows hysteresis, which can be approximately described as a stop hysteresis operator, depicted in Figure S7 and behaving as follows. During the heating phase, the disk contracts and the sliding velocity increases as a linear function of the

contraction ratio λ=(current length)/(maximum length) until the maximum velocity u_{max} = 5.1 μm/s is reached, such velocity is then maintained while the disk contracts further. Notably, since the process occurs at low Reynolds number regime, no inertia is present in the system and the forces acting on the disk (gravitational pull and friction) are always in equilibrium, so the disk acceleration is a consequence of the gradual decrease of the friction coefficient. During the following cooling phase, the disk expands and the sliding velocity decreases as a linear function of λ until a minimum velocity u_{min} is reached, such velocity is then maintained until the disk recovers the initial length. The transition between maximum and minimum velocity, and vice versa, requires a change δ=0.2 in the contraction parameter λ. The value of u_{min} is too small to be reliably measured with the sliding experiment, so in ref.[2] it was estimated to be at most of the order of magnitude of 0.01 μm/s, but possibly slower. As we discuss later, the results of our crawling experiment are in agreement with a value of u_{min} of approximately 0.03 μm/s.

In the same setup, a PEGDA disk shows an intermediate friction coefficient, with a sliding velocity of about 0.77 μm/s. The sliding velocity of the swollen PAA disks is lower, than that of PEGDA disks, indicating higher friction of PAA, compared to PEGDA, which corresponds to the observation of the circular motion of the asymmetric 'T'-shaped crawler in the direction of the PAA leg. At pH 3, in its fully collapsed state, the PAA disks first slide faster as a result of the increased thickness of their lubrication layer, formed by expelled water, and subsequently stop and become stuck, indicating the presence of strong frictional or adhesive forces. This observation appears contradictive to the observed steering direction of the 'T'-shaped crawler, which, at low pH, turns in the direction of the PEGDA arm. As we describe in the main text, the large volumetric change of the PAA segment (to 40 % of its original linear dimension), which occurs isotropically in *x, y* and *z* is the reason. The PAA gel shrinkage in the z-axis and support of the PEGDA section cause it to detach from a surface as can be seen on the confocal image (Figure S4) of a fluorescently labeled crawler at low pH.

Locomotion model for bimaterial crawlers

We present here our model for the locomotion of the PNIPAM-PEGDA microrobot. As the locomotion occurs at low Reynolds number (ca. 10^{-3}) we will neglect inertial terms. Moreover, as discussed previously (ref.[2]), we can neglect also the viscous drag, since it is much smaller compared to the friction with the surface. Hence the evolution of the system will be determined by a balance of friction forces produced by the interaction of the hydrogel with the underlying surface and we therefore can model the crawler as a two-dimensional object, as shown in **Figure S8.**

We assume the stretch ratio in the PNIPAM part to be uniform during the actuation cycle, so that we can denote its length as $\lambda(t)L$ and its width as $w\lambda(t)L$, where $\lambda(t)\leq 1$ is a parameter representing the

contraction of the hydrogel, *L* the length at room temperature and *w* is a shape parameter. We denote with *R* the (constant) length of the passive PEGDA section, while its width is *wL* by construction. Since the model is symmetrical with respect to its longitudinal axis, we obtain a null transversal displacement and null torque, so we study only the longitudinal displacement of the crawler, which we describe with the longitudinal velocity *V(t)* of the passive section, i.e. of the head. As an actuation, we consider a cycle composed of a monotonic contraction and then expansion between λ=1 and $\lambda=\lambda_0<1$. We will focus primarily on contractions in PNIPAM sufficiently large to observe hysteresis in the friction coefficients, namely $\lambda_0<1-\delta$; this is the case also of our experiment, for which λ_0=0.538.

We denote with $\mu(t)$ the friction coefficient per unit area of PNIPAM at a time *t* during the actuation cycle, which is related with the sliding velocity *u(t)* discussed in the previous section through the equation

$$mg\sin\theta = A\,\lambda^2(t)\mu(t)u(t)$$

where *A* is the area of the disk in the rest configuration, *m* the buoyant mass of the disk and θ the tilt angle of the slope. An analogous relation holds for the friction coefficient per unit area μ_{PEGDA} of PEGDA.

Thus the balance of friction forces determining the locomotion of the microrobot is

$$-\mu_{PEGDA}RwLV - \int_0^{\lambda l_{max}} \mu w\lambda L\left[V - \left(L - \frac{s}{\lambda}\right)\dot{\lambda}\right]ds = 0$$

Solving for *V* yields

$$V(t) = \frac{\mu(t)\lambda^2(t)wL^2}{2wL(\mu_{PEGDA}R + \mu(t)\lambda^2(t)L)}L\,\dot{\lambda}(t) = \frac{L\,\dot{\lambda}(t)}{2(\alpha u(t)+1)}$$

where α is a parameter defined as

$$\alpha := \frac{A\mu_{PEGDA}R}{mg\sin\theta\,L}$$

We are interested in the total displacement Δ after one cycle (of duration *T*), namely

$$\Delta = \int_0^T V(t)dt = \int_0^T \frac{L\,\dot{\lambda}(t)}{2(\alpha u(t)+1)}dt = \int_1^{\lambda_0} \frac{L}{2(\alpha u_{heat}(\lambda)+1)}d\lambda + \int_{\lambda_0}^1 \frac{L}{2(\alpha u_{cool}(\lambda)+1)}d\lambda$$

with $u_{heat}(\lambda)$ and $u_{cool}(\lambda)$ denoting the sliding velocity at a certain stage during the heating and cooling phase, see **Figure S7**. Considering large deformations of the PNIPAM, i.e. $\lambda_0<1-\delta$, and noticing that

$$\int_1^{1-\delta} \frac{1}{\alpha u_{heat}(\lambda)+1} d\lambda = -\int_{\lambda_0}^{\lambda_0+\delta} \frac{1}{\alpha u_{cool}(\lambda)+1} d\lambda$$

we obtain

$$\Delta = \int_{1-\delta}^{\lambda_0} \frac{L}{2(\alpha u_{max}+1)} d\lambda + \int_{\lambda_0+\delta}^{1} \frac{L}{2(\alpha u_{min}+1)} d\lambda = \frac{\alpha L(1-\delta-\lambda_0)(u_{max}-u_{min})}{2(\alpha u_{max}+1)(\alpha u_{min}+1)}$$

The value of Δ/L, namely the displacement produced in one cycle rescaled with respect to the length of the active segment, is plotted in Figure S2 in terms of the ratio R/L (appearing in the parameter α) between the lengths of the passive and active segments, showing also the effects of the variability on the λ_0. We observe that for small deformations (i.e. $\lambda_0 > 1-\delta$) the displacement Δ would always be zero, whereas it grows proportionally to $(1-\delta-\lambda_0)$, for deformations above the critical threshold.

We also investigated which ratio R/L would be optimal, maximizing Δ/L. A simple calculation shows that

$$\left(\frac{R}{L}\right)_{\text{optimal}} = \frac{V_{PEGDA}}{\sqrt{u_{max}u_{min}}}$$

The optimal R/L ratio is very sensitive to the parameter u_{min}, which means that, although we cannot obtain a precise *a priori* estimate of the optimal ratio, we can use it to improve *a posteriori* the bounds on the value of u_{min}. As illustrated in Figures S2 and S9, arbitrarily small values of u_{min} would place the performance peak at an arbitrarily large ratio R/L, which does not seem in agreement with the qualitative behavior observed. An optimal ratio of R/L=2, as observed experimentally, would correspond to u_{min} = 0.029 µm/s, which has been selected to plot our Figures. For instance, a lower sliding speed as u_{min} = 0.01 µm/s would produce a peak at R/L=3.54, which would steeply increase for even slower u_{min}. Our crawling model can be therefore used to improve the previous estimate on the maximum friction coefficient μ_{max} of PNIPAM, since we can reasonably exclude the arbitrarily high values of μ_{max} corresponding to sliding speeds much lower than 0.01 µm/s, which were not excluded by the sliding measurements.

Supplementary text S3: Pyranine photoacidity rate and reversibility

To investigate the abilities of macroscopic pH changes mediated by pyranine, we directly measured pH with an electrode. Because we use for crawling experiments 0.3 mm high wells in which the electrode cannot be submerged, we used microtitration wells (12.3 mm high) for pH measurement and diluted the solution (41×) to achieve the same absorbance. Measured pH values are higher (pH =

5.33 before illumination) than with undiluted solution (pH = 4.20) but it is clear, that after 5 minutes of illumination, pH drops by almost two units (Figure S10).

Originally, we intended to use this setup to induce the pH changes locally, which would allow decoupled steering of multiple crawlers. However, the pyranine excitation was too slow to achieve sufficient local pH changes, since the diffusion would be much faster, which we tested experimentally. When only a section of the experimental well was illuminated with the UV (circle 200 µm diameter, circle 50 µm diameter), no local pH changes were observed (detected as deformation of the crawler PAA arm in the illuminated area) and, instead, the pH in the whole well volume was affected (occurring proportionally slower, than when the entire well was illuminated) – i.e. crawlers in and outside the illuminated area were deforming simultaneously. For this reason, we limited our experimentation to the illumination of the whole sample area. Other, faster photoacid molecules were reported recently which would allow for the decoupled steering (ref.[5,6]). Since these are not commercially available, their synthesis and application are the subjects of our next study.

It is also evident from Figure S10, that reversibility of pyranine excitation, detected as a pH increase, is very slow and only partial under our conditions. This irreversibility is most probably caused by redox changes of pyranine. Although it is referred to as highly photo-stable[7], high concentration and long, intensive illumination might induce free-radical mediated decomposition of pyranine resulting in more acidic products[8]. To suppress above-mentioned degradation, we also tried conducting the experiment in an oxygen-free atmosphere, or the addition of a free-radical scavenger (pyrocatechol) which did not help in either case[9].

During illumination with green laser or concomitant solution heating, pyranine apparently forms radicals initiating further polymerization of microrobots, causing their irreversible shrinkage (similar to photopolymerization described in ref.[10]). For this reason, microrobots have been pretreated with mercaptoethanol to remove the double bonds in the gel, that have not been crosslinked during the fabrication[11].

Supplementary Figures

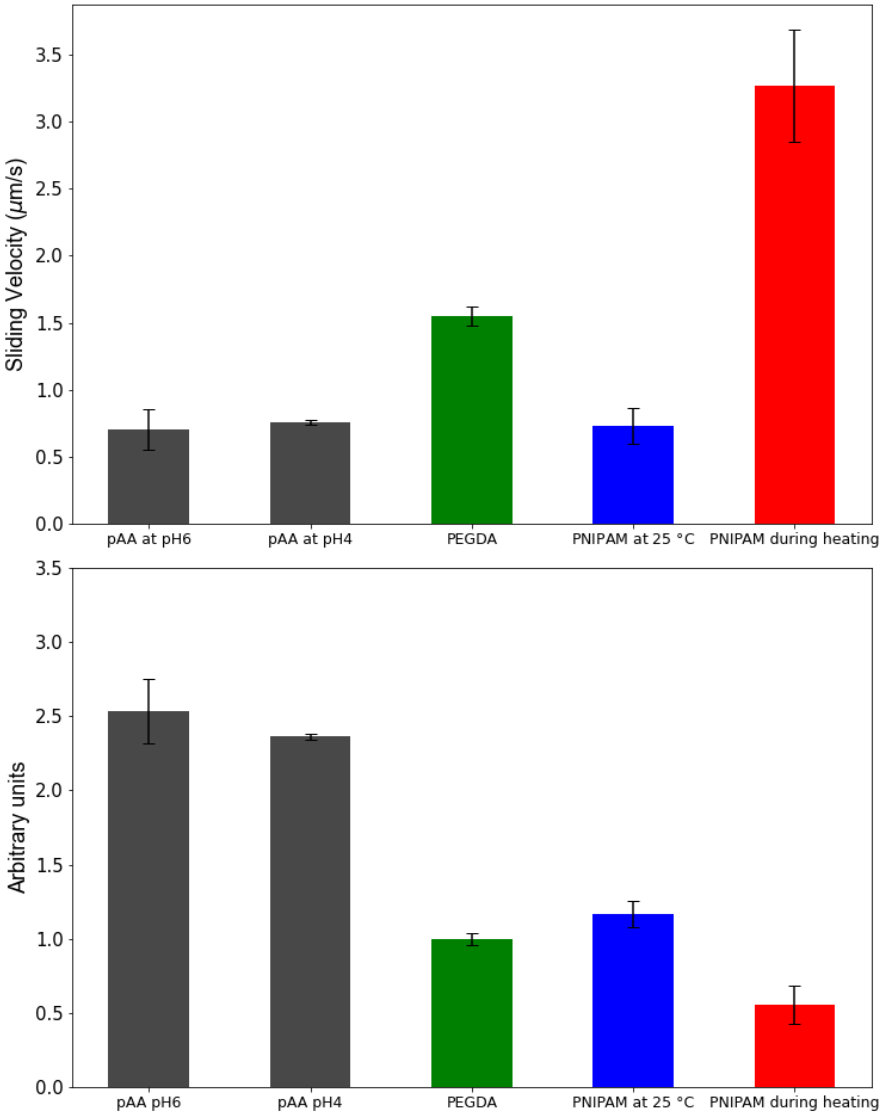

Figure S1. Sliding velocities of gels of various composition (PEGDA, PNIPAM at RT, PNIPAM at 60 °C, PAA at pH = 4 and 6) and relative friction coefficients between substrate (polystyrene) and gels estimated by inversion of the sliding velocity values and relating to the PEGDA reference value corresponding to 1 (Supplementary text S2)

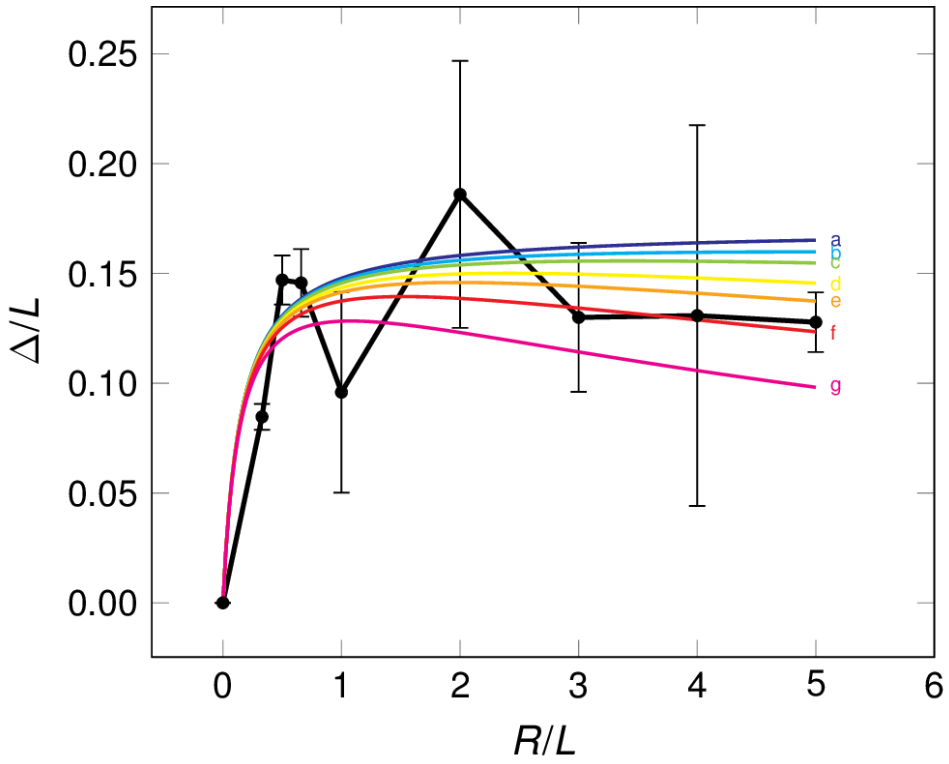

Figure S2. The rescaled displacement for actuation cycle for different values of the lengths ratio *R/L*, measured (black) and predicted for the following different values of u_{min} (in µm/s): 0, i.e. infinite friction (a, blue), 0.005 (b, cyan), 0.01 (c, green), 0.02 (d, yellow), 0.03 (e, orange), 0.05 (f, red), 0.1 (g, purple).

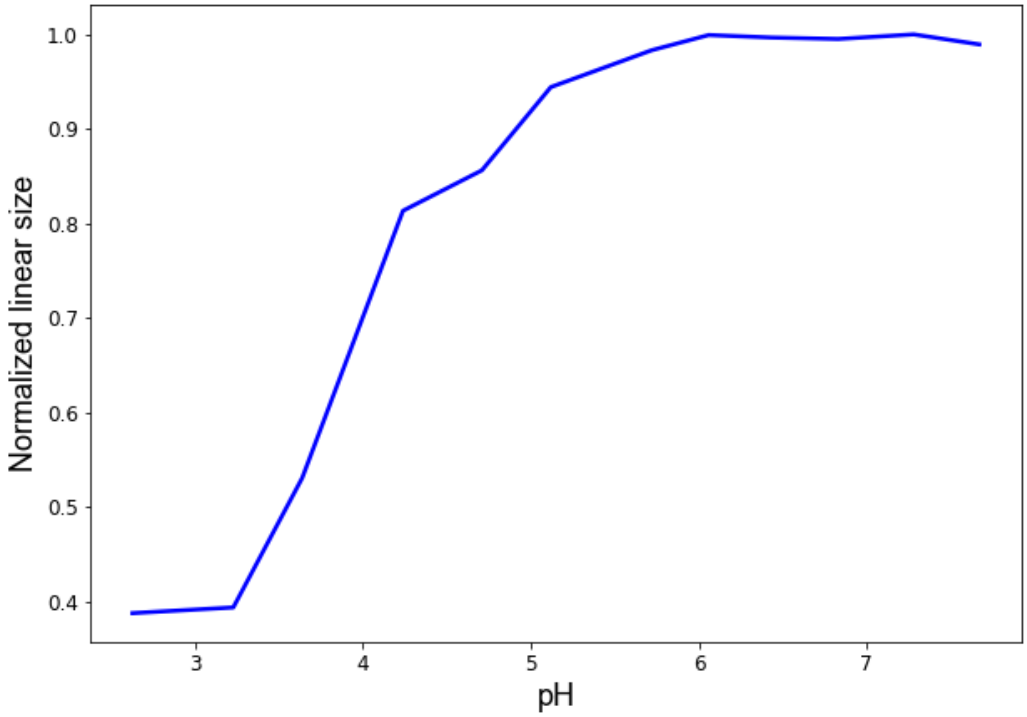

Figure S3. pH dependence of the relative linear size of the PAA-PNIPAM gel – the collapse transition of the gel corresponds to the pH change achieved by illumination of pyranine solution.

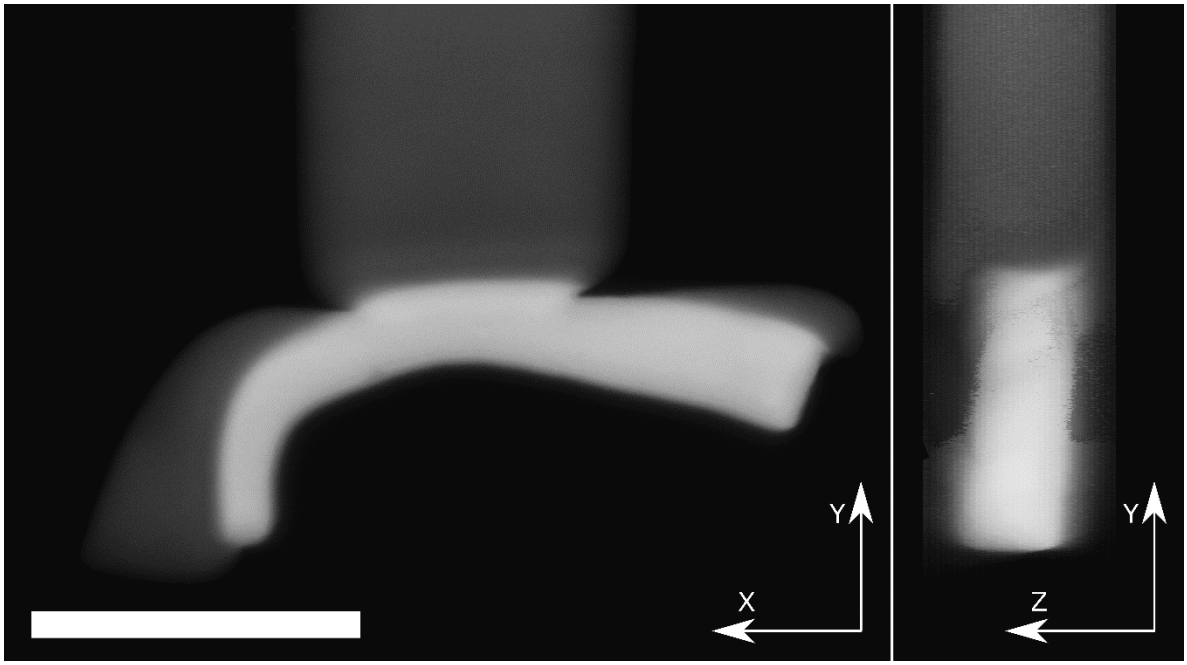

Figure S4. Confocal image of fluorescently labeled crawler – brighter part represents PAA gel and darker part is passive PEGDA gel (Scale bar = 50 µm)

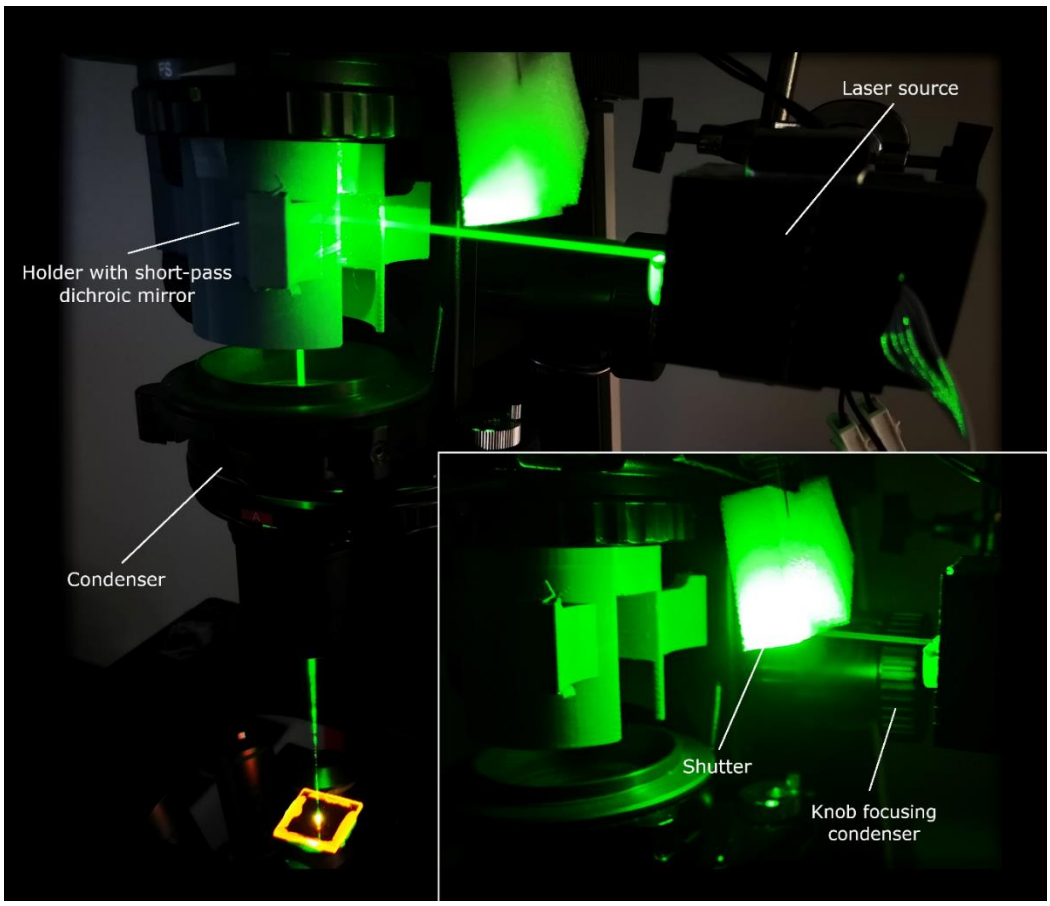

Figure S5. Setup for aiming and focusing green laser. The laser beam is reflected by a dichroic mirror, mounted above the condensor of the inverted microscope by a 3D printed holder. The condenser lens serves for its focusing. The dichroic filter (orange) at the bottom of the image rasts directly above the objective.

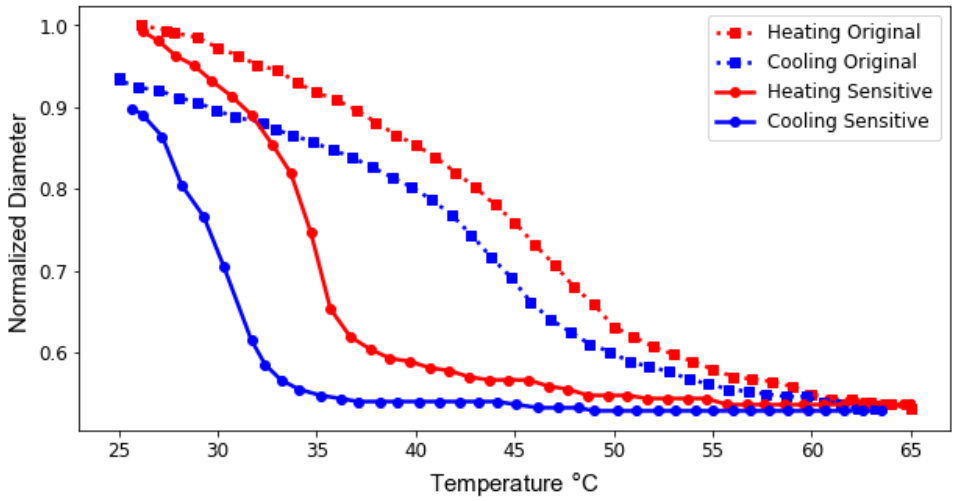

Figure S6. Equilibrium diameter as a function of temperature of the PNIPAM gel crosslinked by PEGDA (circles) and *N,N'*-methylenebisacrylamide (squares). Both gels exhibit hysteresis between heating and cooling, which is commonly observed for PNIPAM (ref.[12,13]).

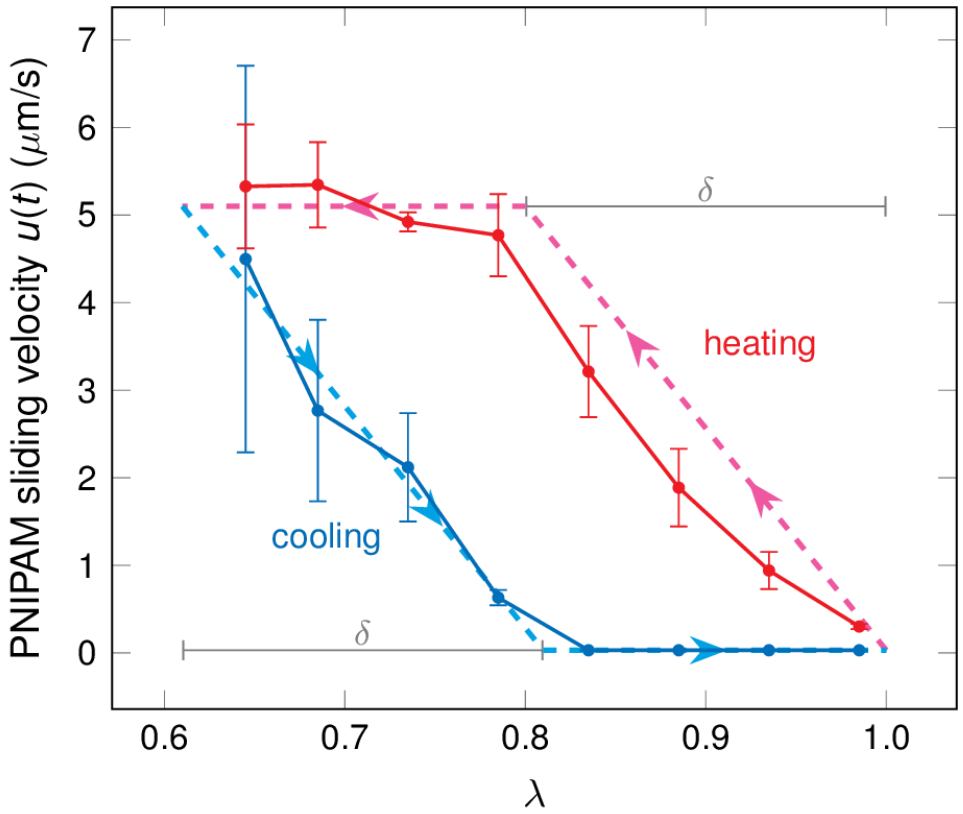

Figure S7. The hysteresis cycle in the sliding velocity of a PNIPAM disk during a heating (red) and cooling (blue) cycle as measured (solid) and the corresponding approximation (dashed) used in our model. Data from[2].

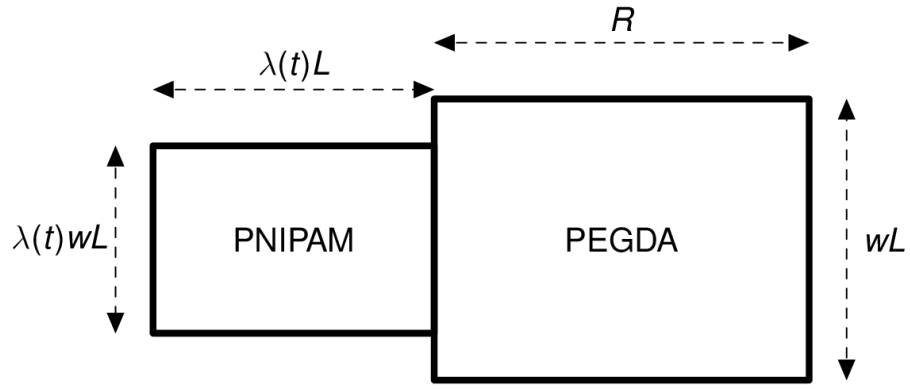

Figure S8. The model of microrobot used in Supplementary text S2.

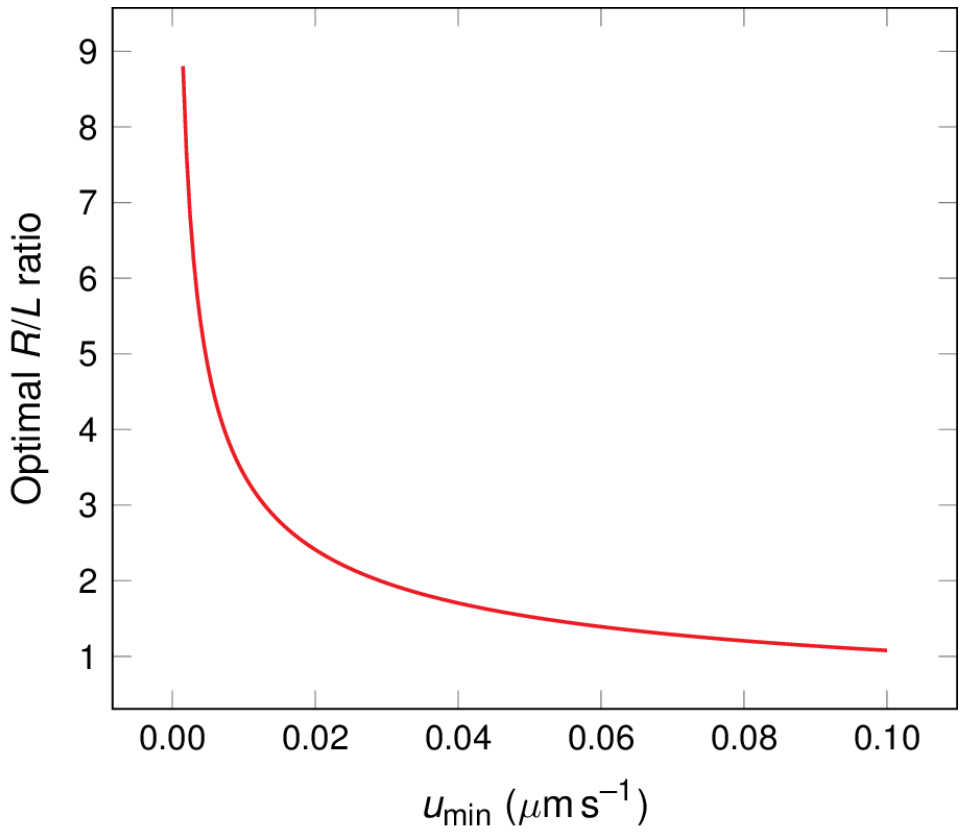

Figure S9. The behavior of the optimal ratio R/L, maximizing the rescaled displacement Δ/L per unit cycle, in terms of the parameter u_{min}.

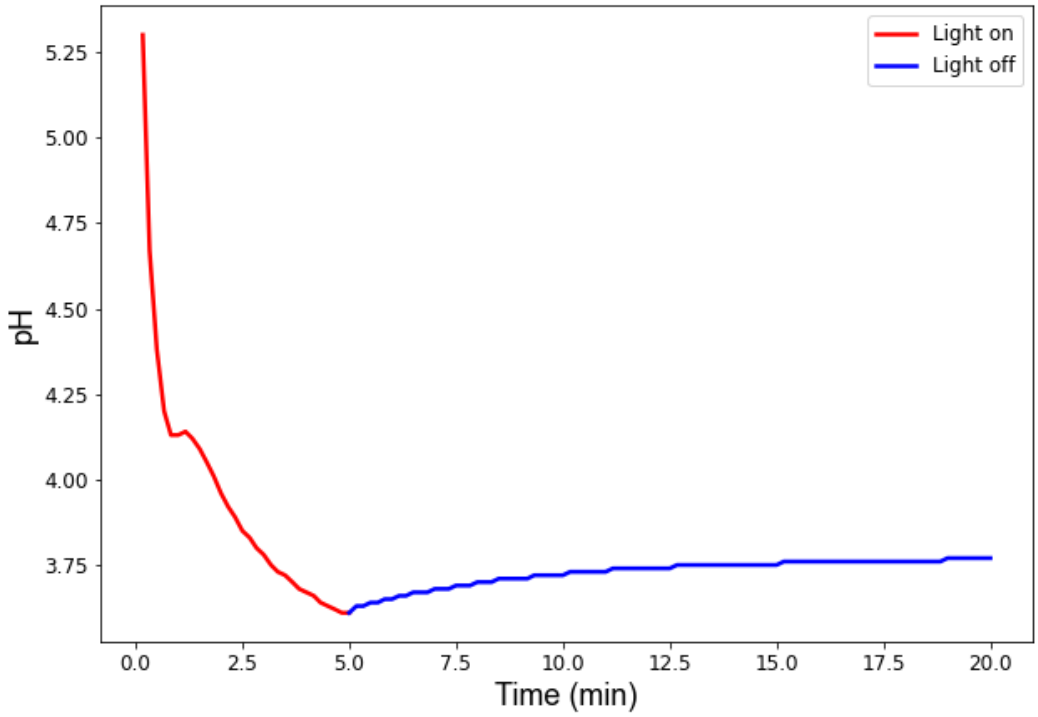

Figure S10. Evolution of pH in pyranine solution upon UV illumination and subsequent dark incubation

Supplementary References

1. Nikoobakht B, El-Sayed MA. Preparation and Growth Mechanism of Gold Nanorods (NRs) Using Seed-Mediated Growth Method. Chem Mater 2003;15(10):1957–1962; doi: 10.1021/cm020732l.

2. Rehor I, Maslen C, Moerman PG, et al. Photoresponsive Hydrogel Microcrawlers Exploit Friction Hysteresis to Crawl by Reciprocal Actuation. Soft Robotics 2020; doi: 10.1089/soro.2019.0169.

3. Mourran A, Zhang H, Vinokur R, et al. Soft Microrobots Employing Nonequilibrium Actuation via Plasmonic Heating. Adv Mater 2017;29(2):n/a-n/a; doi: 10.1002/adma.201604825.

4. Vakkipurath Kodakkadan YN, Maslen C, Cigler P, et al. Friction-directed self-assembly of Janus lithographic microgels into anisotropic 2D structures. Journal of Materials Chemistry B 2021;9(23):4718–4725; doi: 10.1039/D1TB00572C.

5. Halbritter T, Kaiser C, Wachtveitl J, et al. Pyridine–Spiropyran Derivative as a Persistent, Reversible Photoacid in Water. J Org Chem 2017;82(15):8040–8047; doi: 10.1021/acs.joc.7b01268.

6. Finkler B, Spies C, Vester M, et al. Highly photostable “super”-photoacids for ultrasensitive fluorescence spectroscopy. Photochem Photobiol Sci 2014;13(3):548–562; doi: 10.1039/C3PP50404B.

7. Tolbert LM, Solntsev KM. Excited-State Proton Transfer: From Constrained Systems to “Super” Photoacids to Superfast Proton Transfer. Acc Chem Res 2002;35(1):19–27; doi: 10.1021/ar990109f.

8. Velásquez G, Ureta-Zañartu MS, López-Alarcón C, et al. Electrochemical and Spectroscopic Study of Pyranine Fluorescent Probe: Role of Intermediates in Pyranine Oxidation. J Phys Chem B 2011;115(20):6661–6667; doi: 10.1021/jp112057d.

9. Pino E, Campos AM, López-Alarcón C, et al. Free radical scavenging capacity of hydroxycinnamic acids and related compounds. Journal of Physical Organic Chemistry 2006;19(11):759–764; doi: 10.1002/poc.1071.

10. Rehor I, Vreeswijk S van, Vermonden T, et al. Biodegradable Microparticles for Simultaneous Detection of Counterfeit and Deteriorated Edible Products. Small n.d.;13(39):1701804; doi: 10.1002/smll.201701804.

11. Vrba J, Maslen C, Maxova J, et al. An automated platform for assembling light-powered hydrogel microrobots and their subsequent chemical binding. Journal of Computational Science 2021;55:101446; doi: 10.1016/j.jocs.2021.101446.

12. Cheng H, Shen L, Wu C. LLS and FTIR Studies on the Hysteresis in Association and Dissociation of Poly(N-isopropylacrylamide) Chains in Water. Macromolecules 2006;39(6):2325–2329; doi: 10.1021/ma052561m.

13. Lu Y, Zhou K, Ding Y, et al. Origin of hysteresis observed in association and dissociation of polymer chains in water. Physical Chemistry Chemical Physics 2010;12(13):3188; doi: 10.1039/b918969f.